MISSOURI S&T | CURTIS LAWS WILSON LIBRARY
MISSOURI UNIVERSITY OF SCIENCE AND TECHNOLOGY

Scholars' Mine

Masters Theses | Student Theses and Dissertations

Spring 2015

An experimental study of fabrication temperature effect on aqueous extrusion freeform fabrication

Jie Li

Follow this and additional works at: https://scholarsmine.mst.edu/masters_theses

 Part of the Mechanical Engineering Commons

Department:

Recommended Citation

Li, Jie, "An experimental study of fabrication temperature effect on aqueous extrusion freeform fabrication" (2015). *Masters Theses*. 7403.
https://scholarsmine.mst.edu/masters_theses/7403

This thesis is brought to you by Scholars' Mine, a service of the Missouri S&T Library and Learning Resources. This work is protected by U. S. Copyright Law. Unauthorized use including reproduction for redistribution requires the permission of the copyright holder. For more information, please contact scholarsmine@mst.edu.

AN EXPERIMENTAL STUDY OF FABRICATION TEMPERATURE EFFECT ON AQUEOUS EXTRUSION FREEFORM FABRICATION

by

JIE LI

A THESIS

Presented to the Faculty of the Graduate School of the

MISSOURI UNIVERSITY OF SCIENCE AND TECHNOLOGY

In Partial Fulfillment of the Requirements for the Degree

MASTER OF SCIENCE IN MECHANICAL ENGINEERING

2015

Approved by

Ming C. Leu, Advisor
Greg E. Hilmas
Robert G. Landers

© 2015
Jie Li
All Rights Reserved

ABSTRACT

In order to understand the effect of fabrication temperature, a computer controlled 3-D gantry system was used to extrude aqueous alumina paste using Extrusion Freeform Fabrication. The system includes a temperature control subsystem that allows for fabrication of components below the paste's freezing temperature in the range of -10°C to -30°C and a hot plate with temperature in the range of 20°C to 80°C inside a room temperature chamber. Comparisons in terms of relative density, mechanical properties, part accuracy and minimum deposition angle were performed by Extrusion Freeform Fabrication at 40°C plate temperature inside a room temperature chamber and at -20°C plate temperature with a -20°C chamber temperature.

The parts fabricated at 40°C were able to achieve relative density, Young's modulus and flexure strength as high as 96.73%, 311 GPa, and 338 MPa, respectively; the minimum deposition angle achieved was 50^{o} at 38 mm bottom diameter and the parts had 7-14% shrinkage after sintering. In comparison, for the parts fabricated at -20°C, the average relative density, Young's modulus and flexure strength obtained were 91.55%, 280 GPa, and 300 MPa, respectively; parts could be fabricated with a 24^{o} minimum deposition angle at 64 mm bottom diameter and had 10-16% shrinkage after sintering. The hardnesses of parts fabricated at 40°C and fabricated at -20°C were 16.78 GPa and 14.36 GPa, respectively. Microstructures were studied by using SEM to obtain a deeper understanding of the fabrication temperature effect.

ACKNOWLEDGMENTS

First, I would like to express my gratitude to my advisor, Dr. Ming Leu, who brought me into this project and gave me generous support and guidance. I would also like to thank Dr. Greg Hilmas and Dr. Robert Landers sharing their knowledge with me, kindly offering me support for research. They set a significant example with their diligence and outstanding academic performance, teaching me how to be a successful engineer in my future career.

I would like to thank my colleagues from the ceramic engineering department, Dr. Jeremy Watts, Jaci Huebner and Dr. Eric Neuman for offering help and sharing their knowledge.

I would like to thank my fellow students, Krishna Kolan, Aaron Thornton, Amir Ghazanfari, Wenbin Li, Qichang Wang, Cao Dong and Dr. Nannan Guo for their help, support, and friendship throughout my graduate work.

My mother, Lijing He, has been a constant source of support with her words of encouragement and praise.

TABLE OF CONTENTS

LIST OF ILLUSTRATIONS

Figure Page

LIST OF TABLES

1. INTRODUCTION

Since the mid-1980s, solid freeform fabrication (SFF) technology has been developed for its potential use as an efficient and inexpensive manufacturing technique in the production of polymer, metal and ceramic parts in a tool-less fabrication process [1, 2]. At present, SFF techniques for ceramic component fabrication include ink-jet printing [3], stereolithography (SLA) [4], 3D printing (3DP) [5, 6], selective laser sintering (SLS) [7], Robocasting [8] and fused deposition of ceramics (FDC) [9, 10]. These techniques can be classified based on the processes shown in Table 1.1. Most of the SFF techniques for ceramic component fabrication involve the use of high (>40%) concentrations of organic binders that must be removed during post-processing and generate harmful wastes for the environment. One of the extrusion deposition techniques for ceramics is FDC, which is able to print near-fully dense ceramic parts with high surface accuracy. However, FDC uses relatively large amounts of organic chemicals as binders (40-50%) [11].

Table 1.1. SFF techniques for ceramic materials [3-10]

Process	Method	Materials
Selective Laser Sintering (SLS)	Sinter binder mixed in powder bed	Al_2O_3, SiC, $ZrSiO_4$
3D Printing (3DP)	Print binder solution on powder bed	Al_2O_3, Si_3N_4
Stereolithography (SLA)	Cure mixed resins with ceramic particles	SiO_2, PZT, Al_2O_3
Ink-jet Printing	Print colloidal droplets	Al_2O_3, Si_3N_4, ZrO_2
Fused Deposition of Ceramics (FDC)	Print melt particle-filled polymer	Al_2O_3, Si_3N_4, Piezoelectric ceramic
Robocasting (in air/oil)	Print organic/non-organic concentrated colloidal gel	Al_2O_3, PZT, SiO_2

Use of an aqueous process with a lower binder amount could offer a more environmentally friendly alternative than FDC. Robocasting, initially developed at Sandia National Laboratories, is a well-known technology for the fabrication of ceramics and composites. This process can extrude a 50-65% high-solid-loading aqueous slurry containing less than 1% organic binder. For the fabrication of solid and dense samples, Robocasting uses a heating source (40°C hot plate) to increase the slurry's solids loading during extrusion to form a 3D part [8]. The relative density and flexural strength achieved for Al_2O_3 were 93.7% and 310 MPa, respectively [8, 11].

Another aqueous SFF technology is Freeze-form Extrusion Fabrication (FEF), which was developed by researchers at Missouri University of Science and Technology. In FEF, a high solids loading (>50%) aqueous paste containing 1-4 vol% organic additives is deposited inside a freezing chamber (-20°C) to solidify the paste during extrusion. Freeze drying is used to prevent crack formation during the water removal process. The flexural strength achieved for Al_2O_3 was 219 MPa [12, 13].

In this research, a custom-designed 3D gantry system was equipped with a cooling sub-system and a hot plate. This system was used to print aqueous alumina paste via Extrusion Freeform Fabrication at a 40°C plate temperature inside a room temperature chamber and at a -20°C plate temperature in a -20°C temperature chamber to study the effect of fabrication temperature. In this study, the first situation (fabrication at a plate temperature of 40°C inside a room temperature chamber) is referred to as 'at 40°C', and the second situation (fabrication at a plate temperature of -20°C with a -20°C temperature chamber) is denoted as 'at -20°C'.

All experiments used 60% solids loading aqueous Al_2O_3 pastes. The relative density, mechanical properties, part accuracy and minimum deposition angle of Al_2O_3 parts fabricated at different temperatures were tested and recorded. Images from scanning electron microscopy (SEM) and optical microscopy were examined to understand the temperature effects on the microstructure of the fabricated parts.

2. EXPERIMENTAL SETUP

2.1. MACHINE OVERVIEW

The experimental system consists of a motion subsystem, a real-time control subsystem, and extrusion devices. A photograph of the overall system is shown in Fig. 2.1a. The system contains three linear axes Daedal 404 XR (Parker Hannifin, Rohnert Park, CA) driven by three stepper motors (Empire Magnetics, Rohnert Park,CA) and is able to print up to three different materials. In this research, a single extruder is used to extrude aqueous alumina paste. The paste is extruded onto a substrate that moves along the x and y axes. After deposition, the paste is dried via a hot plate, as shown in Fig. 2.1c, or solidifies in a freezing environment, as shown in Fig. 2.1b. When the fabrication of one layer is completed, the gantry moves up by the thickness of one layer. These processing steps are repeated until the entire part is formed.

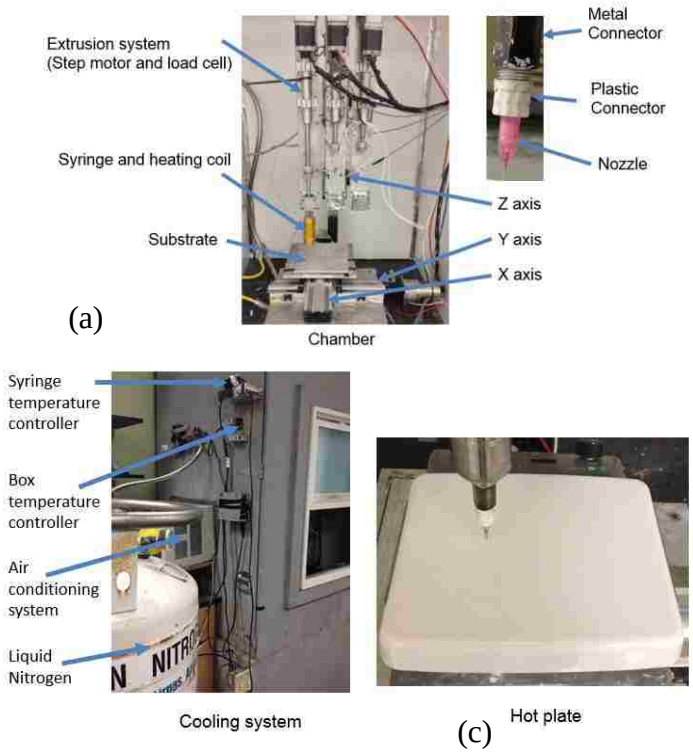

Figure 2.1. Experimental setup of the machine: (a) overview of machine; (b) cooling system and (c) hot plate

2.2. PROCESS PARAMETERS

The process parameters include the extrusion force, layer thickness, filament width, and table speed. A 580 µm diameter plastic nozzle was used for paste extrusion, and the extrusion force was directly related to the extrusion speed.

Calibration of the relationship between the extrusion force and extrusion speed was necessary. A test was performed at 150, 200, 300, 400 and 450 N, and five test runs per reference force were conducted and averaged to verify repeatability. The calibration result is shown in Fig. 2.2, where extrusion speeds of 1.5, 4, 8, 12 and 16 mm/s correspond to 150, 200, 300, 400 and 450 N, respectively. The table speed must match the extrusion speed to avoid under/over-filling. Experiments were carried out at an extrusion force of 400 N and a table speed of 6 mm/s to print a filament with a 0.5 mm layer thickness. Ten single walls were printed to test the filament width. The width was measured using Image J, and the average width was approximately 0.74 mm. Next, a 10% width overlap was tested to reduce the void sizes between two neighboring filaments without overfilling. Skeinforge, an open source software, was used to obtain the motion code for the part fabrication based on these parameters.

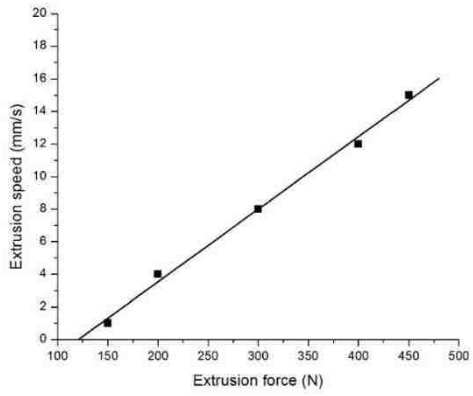

Figure 2.2. Calibration of the relationship between extrusion force and extrusion speed

2.3. MATERIAL CHARACTERIZATION

All of the experiments in the study used 60% solids loading alumina paste. The particle size and size distribution were analyzed using a Microtrac Particle Size Analyzer (S3500, Microtrac, Montgomeryville, PA), as shown in Fig. 2.3. The purpose of this measurement was to define the particle size of a given powder to investigate the effects of particle size on the paste development and sintering process. The particle surface area was measured using a NOVA 2000e instrument (Quantachrome Instruments, Boynton Beach, FL). The Brunauer, Emmett, and Teller (BET) surface area analysis technique was used to determine the surface area of powders. It is important to measure the particle surface area because a higher surface area tends to result in higher densification during sintering but creates additional difficulty in dispersing the particles in the paste preparation [14]. The powder information is listed in Table 2.1.

The paste consisted of a combination of Al_2O_3 powder, glycerol (Aldrich), DARVAN® C-N (ammonium polymethacrylate, Vanderbilt Minerals, LLC), Methocel*F4M (methylcellulose, Dow Chemical Company) and deionized water. The slurry was mixed with Darvan C and glycerol and subsequently ball milled for 10 hours to break up agglomerates and produce a uniform mixture. Darvan C with a negative surface charge was used as a dispersant to mitigate the Van Der Waals forces between particles [15, 16]. Glycerol (20 wt%) was used to prevent the growth of large ice crystals and freezing defects associated with water crystallization [17]. Methocel was dissolved in water at 70°C after 5 minutes of mechanical stirring to form a 60 vol% solids loading paste and was chosen as a binder to increase the paste viscosity and assist in the formation of a stronger green body after drying. Finally, a vacuum mixer (Whip Mix, Model F) was used to remove air bubbles by degassing for 10 minutes.

Table 2.1. Powder characterization

Name	Company	Particle Size (μm)	Surface Area (m^2/g)	Purity
Al_2O_3 (A-16SG)	ALMATIS	0.34	9.44	99.8%

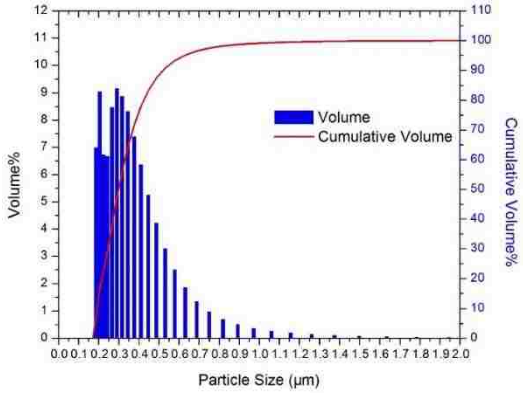

Figure 2.3. Particle size distribution

2.4. POST PROCESSING

Water in the test bars fabricated at -20°C was removed via sublimation using a freeze dryer (Virits, Model Genesis 25XL, Gardiner, NY). The temperature was manually set to -10°C, and the pressure was held at 1.7 Pa (13 mTorr) for three days. On the other hand, the water inside the paste was evaporated at 40°C to increase solids loading, which provides the strength needed to form 3D parts.

A dried alumina bar was used to perform binder removal by heating from room temperature to 1,000°C in air at a rate of 10°C/minute. The weight of binder versus temperature relationship indicated that the maximum mass change was approximately 5.31%, and the binder removal ended at approximately 500°C (see Fig. 2.4). This process could be divided into three stages. First, any remaining residual water and low melting point additives were removed from room temperature to 121°C. The next stage from 121°C to 230°C removed the glycerol. Finally, the higher molecular weight binders were removed in the range of 230°C to 432°C.

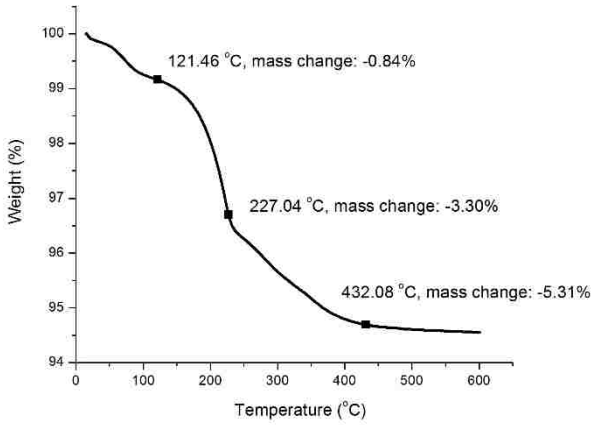

Figure 2.4. TGA of Al_2O_3 part with 20 wt% glycerol

The sintering test results are listed in Table 2.2, and the relative density of the sintered samples was measured using Archimedes method. Pressed pellets were used to test the sintering schedule. The highest relative density averaged over five samples was 97.8%.

Table 2.2. Results of sintering test

Temperature	Holding Time	Atmoshpere	Heating Rate	Relative Density
1500°C	90 minutes	Air	10°C/minute	92.09%
1550°C	90 minutes	Air	10°C/minute	95.45%
1550°C	2 hours	Air	10°C/minute	97.8%

The thermogravimetric analysis (TGA) results (see Fig. 2.4) and the results of the sintering test (see Table 2.2) were used to determine the post-processing schedule, as shown in Fig. 2.5. After drying, the samples were pyrolyzed to remove the remaining organics using a 0.5°C/minute ramp up to 500°C with a hold of 2 hours. Next, the

samples were sintered to 1,550°C using a heating rate of 10°C/minute, held for 2 hours, and then cooled to room temperature.

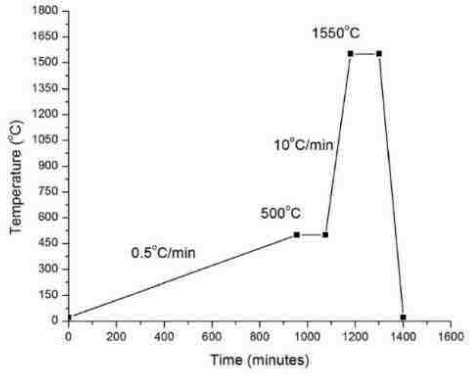

Figure 2.5. Binder removal and sintering schedule

2.5. MECHANICAL PROPERTIES AND MICROSTRUCTURE

Test samples were printed at both 40°C and -20°C. The fabricated samples were ground by diamond machining according to ASTM C-1161 standard "B" bars (4x3x45 mm^3) and ASTM C-1161 standard "A" bars (2x1.5x20 mm^3). Four-point bending tests were performed on a screw-driven mechanical frame (Instron, Model 5881, Norwood, MA) to test the flexural strength and elastic modulus.

A micro-hardness tester (Struers, Model Duramin-5, Ballerup, Denmark) was used to measure hardness. The hardness of standard A bars fabricated at 40°C and -20°C were measured using a load of 1 kg, and five measurements were collected for each specimen on a 0.25 μm diamond polished surface.

Each method (bars fabricated at 40°C, -20°C, and -20°C without using a nozzle) used the same batch paste to print three bars to test the green body density. After drying and binder removal, the Archimedes method (in water) was used to measure the green body density and relative density after sintering.

The microstructures of bars fabricated at 40°C, -20°C, and -20°C with a 0°C substrate temperature, -20°C without using a nozzle and pressed pellets were studied to better understand the effect of printing flaws and the formation of ice crystal voids. Samples were polished to a 0.25 μm surface finish, and SEM (Jeol 330, Peabody, MA) was used to examine the microstructure of each sample.

3. RESULTS AND DISCUSSION

3.1. TEMPERATURE EFFECTS

The drying rate was insufficient for paste printing on a room temperature plate in a room temperature chamber. If the paste is not sufficiently solidified and remains in a liquid-solid state, a large 3D part under fabrication will deform or even collapse. In contrast, the drying rate of the extruded materials on a 60°C plate inside a room temperature chamber was significantly higher than that when printing at 40°C. Moisture in the body was distributed unevenly due to the temperature difference in the parts, and the non-uniform drying led to warping and cracking, as illustrated in Fig. 3.1.

Figure 3.1. Warping at 60^{o}C

A large pore (see Fig. 3.2a) remained inside the bar when the part was fabricated at 40°C. The short waiting time (no additional waiting time for a deposited layer) for each layer led to this large pore because the pore size was larger than one filament and the boundary was smooth. Thus, the printing process was altered slightly to increase the waiting time by a factor of three (approximately 210 s) for each layer. After the machine printed one layer of the first part, it moved to print a layer of second and third parts. After printing one layer of the other two parts, the machine returned to print the next layer of the first part. This process eliminated the pore entirely (see Fig. 3.2b), and this method not only increased the building time for one layer but also reduced fabrication time. In addition, the required waiting time for which a single semi-solid filament (0.5x0.74x60 mm^3) became a solid filament was estimated after deposition and was approximately 20

second at 40°C. The required waiting time of 20 s led to filament fusion with the previous filament and removed the flaws between filaments, as shown in Fig. 3.2b.

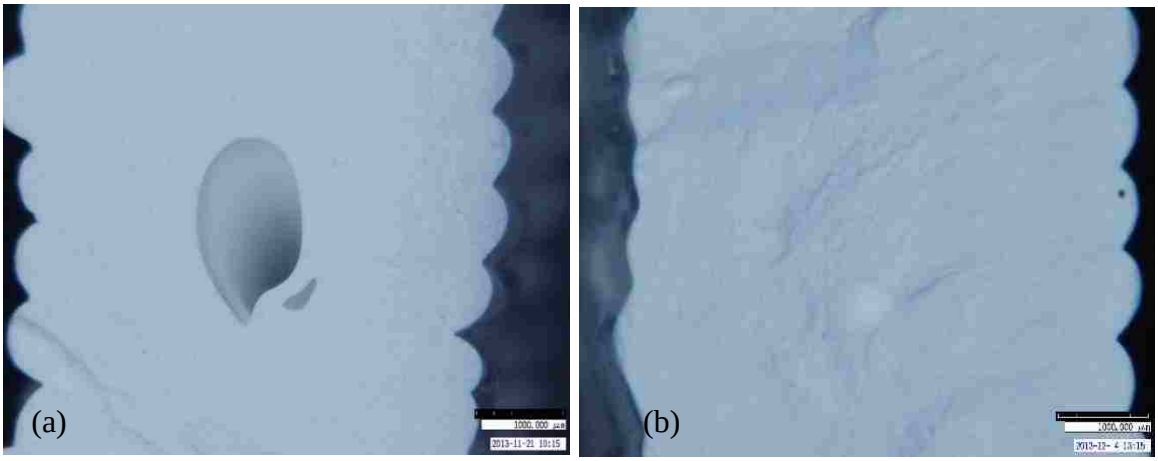

Figure 3.2. Cross-section of a green body fabricated at 40°C: (a) short waiting time for each layer and (b) 210 s waiting time for each layer

Ten bars (6x7x60 mm^3) were fabricated at 40°C and ground to the standard B bar size. The average flexural strength for bars fabricated at 40°C was 253 MPa, and the average elastic modulus was 327 GPa, as listed in Table 3.1. The flexural strength of those parts was considerably lower than that of the pressed bars (370-390 MPa). A small amount of printing flaws and air bubbles in the paste (see Fig. 3.3) caused a porosity of approximately 3%, which reduced the strength considerably. Ten additional single walls with only one filament at each layer were fabricated to eliminate printing flaws. The difference between the bar's relative density and the printing-flaw-free single wall's relative density was less than 1% (see Table 3.1). Compared with the relative density of pressed pellets (97.8%), the air bubble in the paste was the main reason for the approximately 3% more porosity of parts fabricated at 40°C.

Table 3.1. Mechanical properties and relative density of bars fabricated at 40°C

#	Flexural Strength (MPa)	Young's Modulus (GPa)	Relative Density (%)	Relative Density of Single Walls （%）
1	327	352	94.40	93.63
2	290	333	96.30	95.01
3	276	341	92.20	94.81
4	268	330	92.62	94.73
5	262	349	94.03	94.47
6	246	320	94.14	94.86
7	244	286	92.24	94.55
8	234	316	94.04	94.34
9	207	306	93.67	94.32
10	177	337	94.15	96.85
Average	253	327	93.78	94.76
Standard Deviation	42	20	1.22	0.83

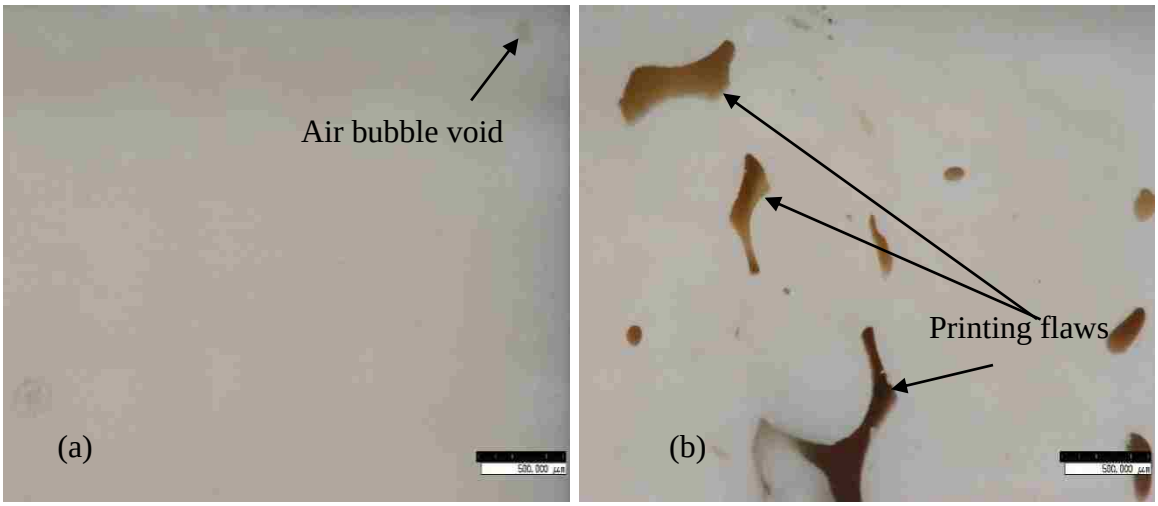

Figure 3.3. Cross-section of bars fabricated at 40°C: (a) bar #1 and (b) bar #10 from Table 3.1

A heating coil (see Fig. 2.1a) was used for chamber temperatures below 0°C to maintain the paste warm at room temperature. Two bars were fabricated at a -20°C chamber temperature with a 0°C plate temperature. The relative density, flexure strength and Young's modulus of the bars were 86.5%, 48 MPa and 101 GPa, respectively. The mechanical properties of the bar were inferior to those printed at a -20°C plate temperature because of the large size ice voids that formed, as illustrated in Fig. 3.4.

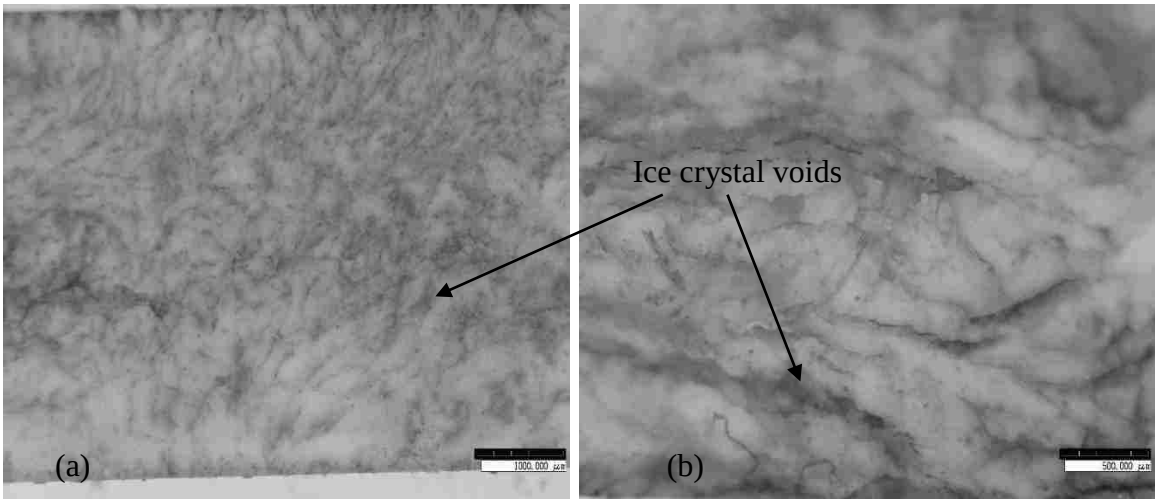

Figure 3.4. Bars fabricated at a 0°C plate temperature: (a) side view and (b) cross-sectional view

Another critical issue for printing at chamber temperatures below 0°C was clogging. In this research, clogging refers to the state in which the paste could not be extruded properly and either slowed or completely halted extrusion. This issue is illustrated in Fig. 3.5. In this figure, the paste extrusion has halted, and the part has failed.

Clogging often occurred because the paste froze inside the nozzle before it was extruded. A test of increasing extrusion force was performed to understand this clogging problem. Extrusion forces were tested at 150, 200, 300 and 400 N. The table speed ranged from 2 to 14 mm/s and matched the extrusion speed. This test revealed that a lower extrusion force led to more frequent clogging than a higher extrusion force. At a high extrusion force, warm paste (approximately 20°C) could pass through the nozzle

faster and was thus less likely to freeze inside the nozzle. However, the paste remains at the nozzle tip for a longer period of time if extrusion is slow, and thus, clogging becomes more critical.

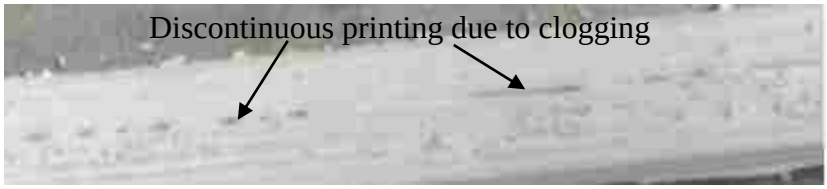

Figure 3.5. Clogging problem

Six bars (6x7x60 mm^3) were fabricated at -20°C and ground to the standard B bar size. The average flexural strength of bars fabricated at -20°C was 153 MPa, and the average elastic modulus was 327 GPa (see Table 3.2). Ice crystals, printing flaws, and air bubbles in the paste were primarily responsible for this low flexural strength. Bars fabricated at -20°C contained more flaws (Fig. 3.6) than those fabricated at 40°C. Two factors were responsible for this increased number of flaws. First, the clogging that occurred led to discontinued printing and voids. Second, the paste that was fabricated at -20°C solidified faster than the paste fabricated at 40°C. The extruded ceramic paste could freeze at -20°C, and the required waiting time for one filament (0.5x0.74x60 mm^3) was estimated and approximately 10 second. The 10 second required waiting time was shorter than the time required for a filament to overlap a previous filament, and thus, this process was unable to fill the voids between filaments as adequately as printing at 40°C. The pore at the top of the layer was removed by overlapping, but the pore at the bottom of the layer could remain, as shown in Fig. 3.6a. Single walls were used to test the density without printing flaws and indicated that ice crystal voids also contributed to the lower density.

Table 3.2. Mechanical properties and relative density of bars fabricated at -20°C

#	Flexural Strength (MPa)	Young's Modulus (GPa)	Relative Density (%)	Relative Density of Single Walls （%）
1	192	242	88.74	86.52
2	166	217	86.91	87.58
3	161	274	88.83	87.30
4	154	244	88.06	84.67
5	132	246	89.12	86.36
6	116	197	85.74	86.71
Average	153	237	87.90	86.52
Standard Deviation	24	24	1.21	0.93

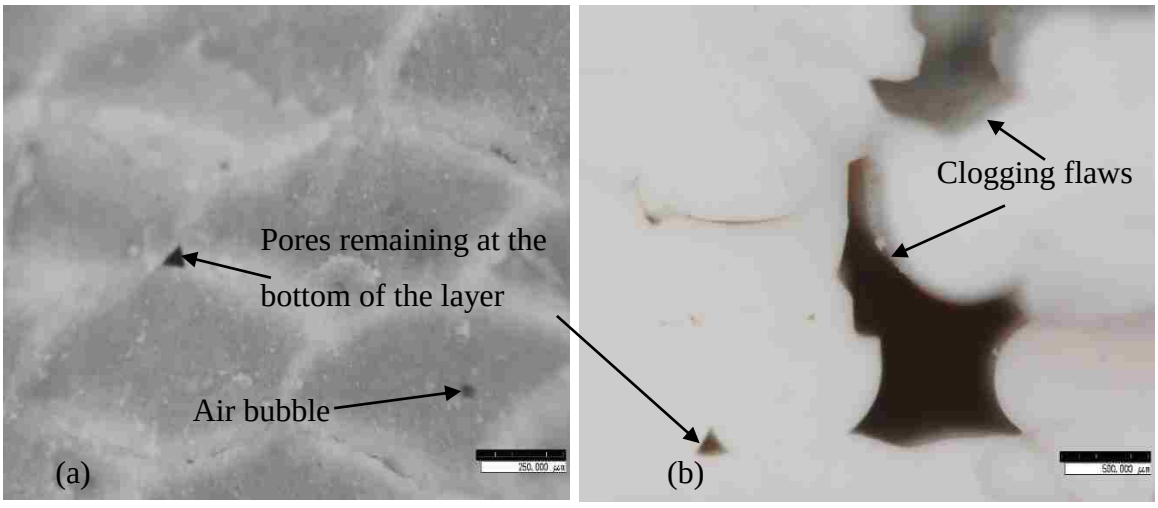

Figure 3.6. Cross-section of bars fabricated at -20°C: (a) bar #1 and (b) bar #6 from Table 3.4

Five ‘big’ bars were fabricated at -20°C without using a nozzle to avoid printing flaws. These ‘big’ bars only contained one filament and were printed directly from a syringe; the size was approximately 10x10x60 mm^3 after deposition. After post-processing, the sample was ground to standard B bar size.

The ‘big’ bars did not contain any printing flaws, but the flexural strength and elastic modulus of these bars (listed in Table 3.3) were even lower than those of the bars fabricated with a nozzle at -20°C (Table 3.2). Thus, the low strength could be related to the filament size. This relatively large filament contained an uneven temperature gradient inside. The temperatures inside the filament and at the surface were measured (see Fig. 3.7) using a thermometer. As shown in Figure 3.7, the temperature inside the large filament was approximately -15°C when the filament’s surface temperature was -20°C. Ice crystal formation was also observed, as shown in Fig. 3.8. It is reasonable to believe that larger crystal sizes were formed when the temperature was warmer (between 0°C and -20°C). Details are provided and discussed in Section 3.4.

Table 3.3. Mechanical properties and relative density of bars fabricated at -20°C without using a nozzle

#	Flexural Strength (MPa)	Young’s Modulus (GPa)	Relative Density (%)
1	122	186	86.19
2	104	210	85.23
3	77	179	85.01
4	69	139	86.07
5	60	149	85.46
Average	86	173	85.59
Standard Deviation	23	26	0.46

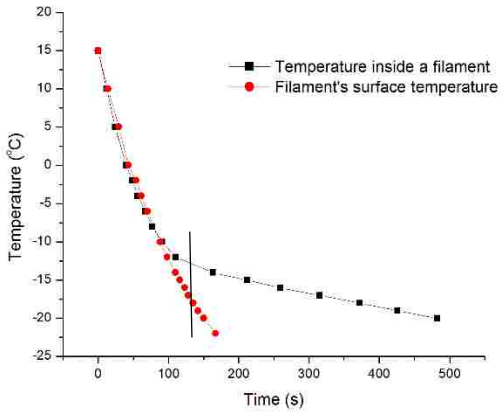

Figure 3.7. Demonstration of a non-uniform temperature inside the filament fabricated at -20°C without using a nozzle

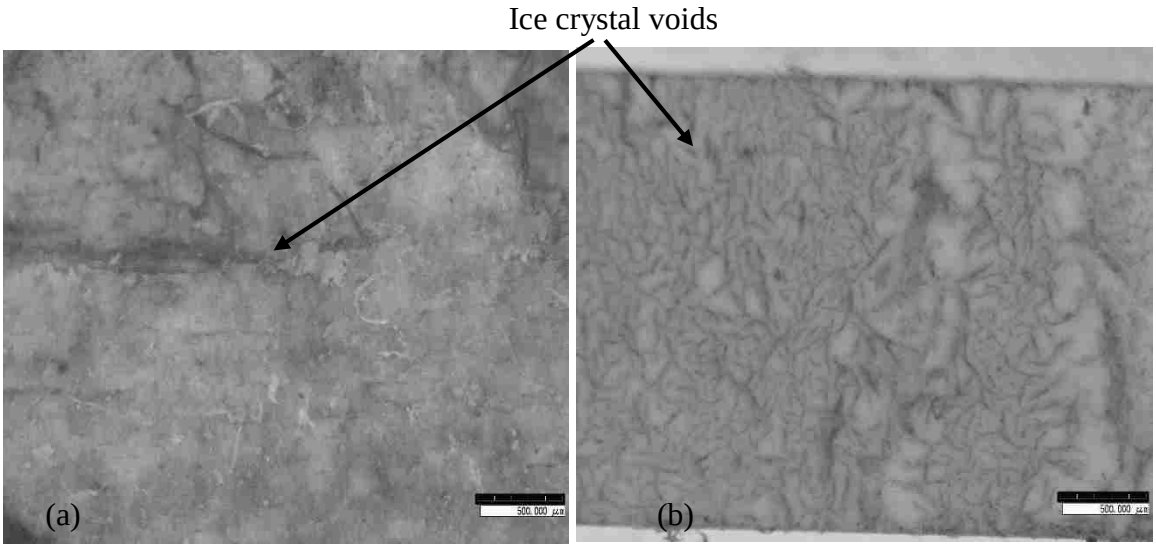

Figure 3.8. Bars fabricated at -20°C without using a nozzle: (a) cross-section and (b) side view

Figure 3.9 provides a comparison of the flexural strengths and relative densities for bars fabricated under three different conditions. The relative density of bars fabricated at 40°C was 94.76%, which was higher than that of bars fabricated at -20°C with and without using a nozzle (86.52% and 85.59%, respectively). The relative density of bars

fabricated at -20°C with and without using a nozzle did not exhibit a considerable difference (1%). Comparing the green body density of bars fabricated at 40°C, -20°C and -20°C without using a nozzle, the bars with ice crystal voids exhibited a lower density. However, the flexural strength of bars fabricated at -20°C without using a nozzle was 40% lower than the flexural strength of bars fabricated at -20°C with using a nozzle (see Fig. 3.9a).

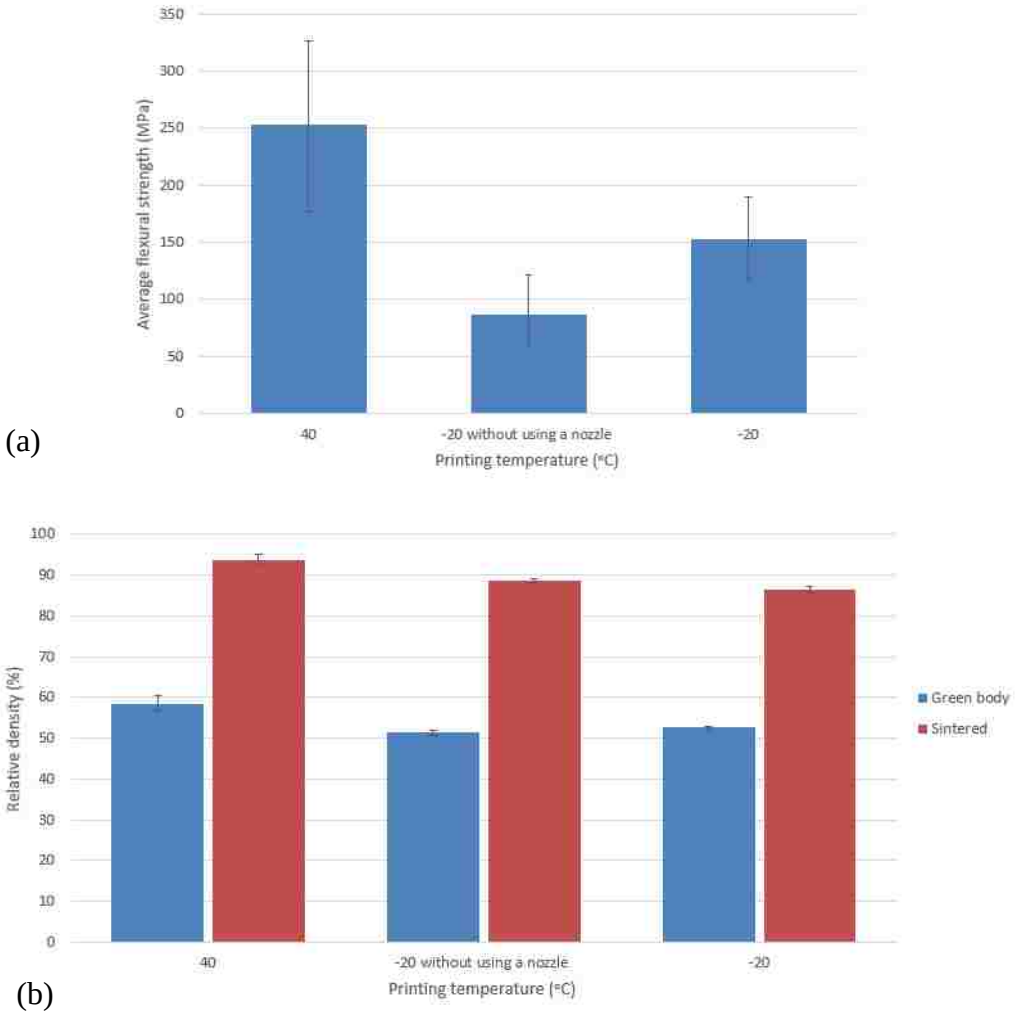

Figure 3.9. Comparison of the (a) mechanical properties and (b) relative density of parts fabricated by three different methods

3.2. PART ACCURACY AND MINIMUM DEPOSITION ANGLE

Single walls (Fig. 3.10) and bars (Fig. 3.11) were printed at 40°C and -20°C to compare part accuracy. The surfaces of both single-wall specimens were rough due to a general problem with the extrusion deposition technique. The dimensions were measured for the green bodies (after drying) and sintered parts, as listed in Table 3.4.

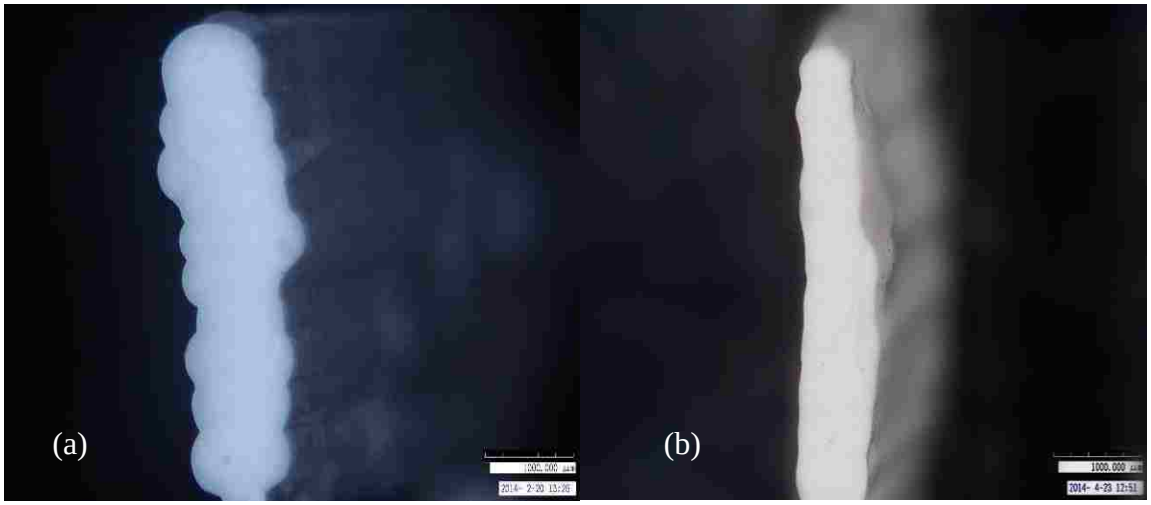

Figure 3.10. Cross-section single walls: (a) fabricated at 40^{o}C and (b) fabricated at -20^{o}C

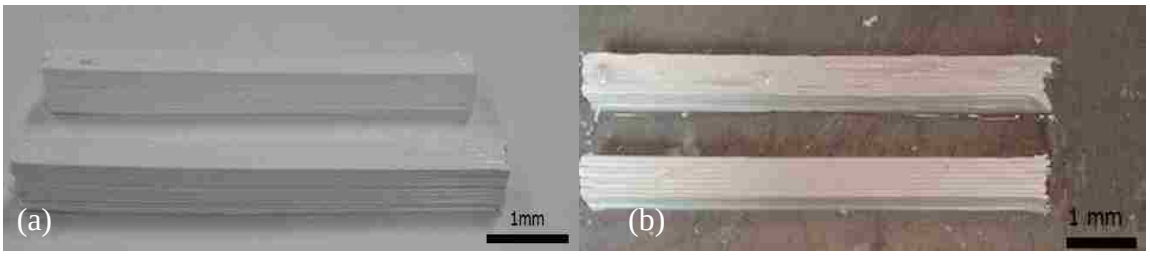

Figure 3.11. Printed bars: (a) fabricated at 40^{o}C and (b) fabricated at -20^{o}C

Table 3.4. Shrinkage in the green body and sintered part

		W (mm)	H (mm)	L (mm)
CAD		5.6	7.8	70
Printed at 40°C	Green body size	6.03 ±0.12	8.03±0.13	71.12±0.12
	Linear shrinkage of green body	-7.68±2.06%	-2.91±01.64%	-1.60±0.18%
	After sintering size	5.05±0.16	7.24±0.03	60.54±0.16
	Linear shrinkage after sintering	9.88±2.90%	7.22±0.44%	13.51±0.23%
Printed at -20°C	Green body size	6.17±0.10	8.19±0.02	72.37±0.20
	Linear shrinkage of green body	-10.24±1.69%	-5.04±0.26%	-3.39±0.29%
	After sintering size	5.04±0.15	7.00±0.11	58.78±0.21
	Linear shrinkage after sintering	10.06±2.70%	10.21±1.39%	16.02±0.29%

The expansion in the width was larger in the green body because the width of the filaments varied. Parts fabricated at -20°C experienced 1.5-3% more expansion than parts fabricated at 40°C because each filament contained approximately 40 vol% water and freezing of water increased the total volume. The freezing of water increased the paste volume by approximately 7%; the volume of paste should increase by 40% (solids loading) x 7%=2.8%, and the measured value was 3%. Therefore, these numbers explain the increased expansion of the bars fabricated at -20°C compared to bars fabricated at 40°C.

The minimum deposition angle refers to the angle that can be achieved between the substrate and the slope of a hollow cone without collapse, as illustrated in Fig. 3.12a. This angle reflects the capability of the Extrusion Freeform Fabrication process in building a 3D part without the use of support material [18].

In this study, two sets of tests were conducted to fabricate cones with different bottom diameters to determine the minimum deposit angle. In each set of tests, hollow cones were fabricated using bottom diameters of 38, 51 and 64 mm. The cone angle was varied from 60° to 20° by 5° decrements to measure the failure angle of the cone, and the angle was subsequently increased from the failure angle by 2° increments to determine

the minimum deposition angle. The part was printed with a 6 mm/s table speed. For bottom diameters of 38, 51 and 64 mm, the waiting times for one layer at the bottom of the cone were approximately 19.9, 26.7 and 33.5 second, respectively; for the layer at the middle height of the cone, the waiting times for one layer were approximately 9.9, 13.3 and 16.7 second, respectively. As shown in Table 3.5, the parts printed at -20°C had a smaller minimum deposition angle than those printed at 40°C. Comparing the parts fabricated at 40°C, each filament solidifies faster at -20°C and thus provides the strength needed to prevent part collapse. The minimum deposition angle decreases with increasing bottom diameter at -20°C because a larger bottom diameter has a longer waiting time for one layer. However, the minimum deposition angle increases with a decreasing bottom diameter at 40°C because a larger bottom diameter requires the cone to support more weight. Additionally, as discussed in the previous section, the required waiting time at 40°C was approximately 20 s, and therefore, the increase in diameter did not have a significant effect on reducing the minimum deposition angle; the cone mainly failed at the middle or top of the cone because those layers did not undergo a sufficient waiting time to solidify and provide the strength necessary to form a hollow cone.

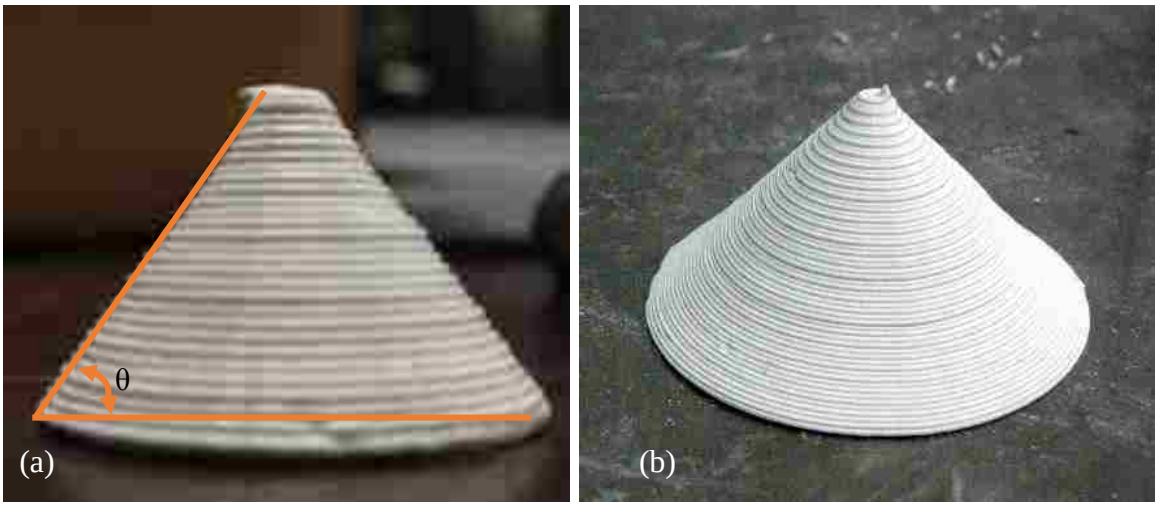

Figure 3.12. Hollow cone successfully built by: (a) fabricated at 40°C and (b) fabricated at -20°C [18].

Table 3.5. Minimum deposition test results

	Bottom Diameter = 38 (mm)	Bottom Diameter = 51 (mm)	Bottom Diameter = 64 (mm)
	Minimum deposition angle θ (°)		
Fabrication at 40°C	50	52	55
Fabrication at -20°C[18]	28	26	24

3.3. RELATIVE DENSITY AND MECHANICAL PROPERTIES

The bars fabricated at 40°C and -20°C had a green density of 58.49% and 51.35%, respectively. Ten standard A bars were fabricated at both 40°C and -20°C and were subjected to the same post-processing. As shown in Tables 3.6 and 3.7, bars fabricated at -20°C achieved an average strength of 300 MPa, whereas the average strength of bars fabricated at 40°C was 338 MPa.

Table 3.6. Mechanical properties and relative density of standard A bars fabricated at -20°C

#	Flexural Strength (MPa)	Young's Modulus (GPa)	Relative Density (%)
1	334	261	90.48
2	325	259	93.32
3	303	356	91.34
4	269	285	91.41
5	268	240	91.18
Average	300	280	91.55
Standard Deviation	28	40	0.95

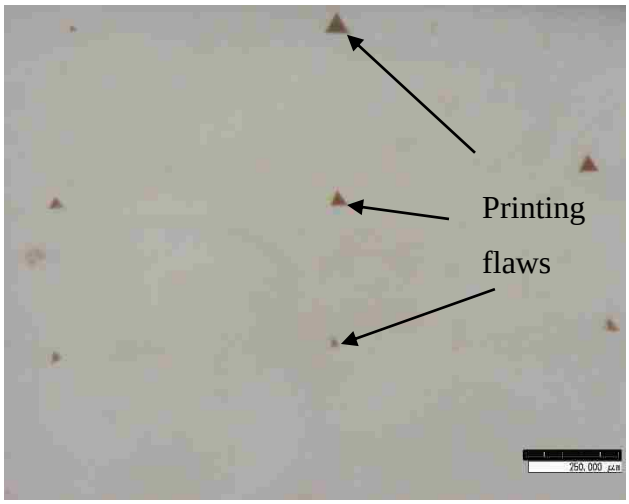

Figure 3.13. Cross-section of bar #3 from Table 3.7

Table 3.7. Mechanical properties and relative density of standard A bars fabricated at 40°C

#	Flexural Strength (MPa)	Young's Modulus (GPa)	Relative Density (%)
1	406	273	97.18
2	361	316	97.11
3	348	308	96.15
4	346	353	97.31
5	232	306	95.92
Average	338	311	96.73
Standard Deviation	57	25	0.58

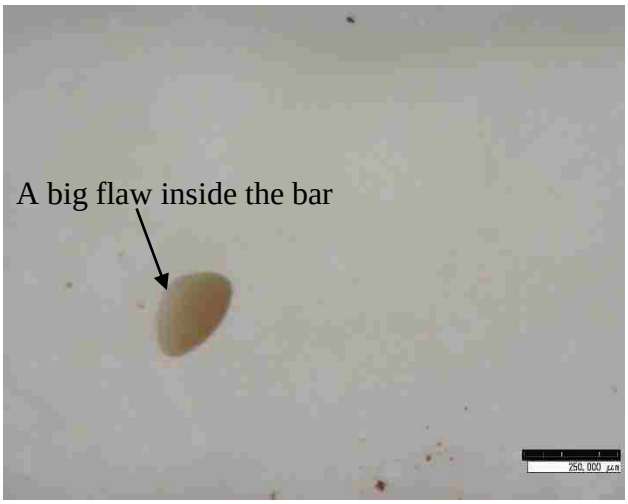

Figure 3.14. Cross-section of bar #5 from Table 3.8

The theoretical flaw size was calculated using Equation (1), which is the Griffith criterion. The fracture toughness was assumed to be 4 MPa*$m^{1/2}$ [19] and a shape factor that is characteristic of joined particles, the Griffith criterion is

$$\sigma_f = \frac{K_{IC}}{Y\sqrt{c}} \quad (1)$$

where K_{IC} is the fracture toughness, Y= $\pi^{1/2}$ and c is one half of the maximum flaw size.

The calculated and measured maximum flaw sizes for bars fabricated at -20°C and 40°C are given in Table 3.8 based on the results of the standard A bar test (see Tables 3.6 and 3.7). The measured size was not same as the calculated size because the fracture toughness might not be suitable for all parts. However, the calculated flaw size provides a general tendency that can be used to find the maximum flaw size. One sample of the maximum flaw size for bars fabricated at -20°C and 40°C is illustrated in Figs. 3.13 and 3.14, respectively. Based on Table 3.8, the flaws for bars fabricated at -20°C were the size of printing flaws; for bars fabricated at 40°C, the flaws shown in bars #3 and #4 were air bubbles. As noted in Section 3.1, the filaments solidified faster at -20°C and were unable to fill the voids between the filaments entirely. Figure 3.13 shows the printing

flaws, and Fig. 3.14 shows a large flaw that might be due to an agglomerated binder or air bubble. This flaw considerably reduced the flexural strength to 232 MPa.

Table 3.8. Calculated and measured maximum flaw size for the standard A bar

Standard A Bar	Calculated Maximum Flaw Size (μm)	Measured Maximum Flaw Size (μm)
Bars fabricated at 40°C	Bar #3: 84.29	Bar #3: 54
	Bar #4: 85.30	Bar #4: 84
	Bar #5: 189.28	Bar #5:177
Bars fabricated at -20°C	Bar #2: 96.75	Bar #2: 66
	Bar #3: 110.78	Bar #3: 91
	Bar #4: 141.31	Bar #4: 116

Assuming a modulus of 380 GPa [20] for 100% density Al_2O_3. The theoretical elastic modulus was calculated using Nielsen's relationship of elasticity for porous ceramic materials. Nielsen's relationship is

$$E = E_0 \frac{(1-P)^2}{1+\left(\frac{1}{\rho}-1\right)P} \quad (2)$$

where E_0 is the pore-free elastic modulus, P is the volume percent of porosity and ρ is Nielsen's shape factor (0.4).

Based on the standard A bar results (see Tables 3.6 and 3.7), the theoretical elastic modulus for bars fabricated at 40°C with 3.27% porosity was 339 GPa, and the bars fabricated at -20°C with 8.5% porosity should have a 282 GPa theoretical elastic

modulus. The 28 GPa difference between the measured and theoretical elastic moduli for bars fabricated at 40°C was approximately equal to the 25 GPa deviation of the measurement; the measured 280 GPa elastic modulus for bars fabricated at -20°C was approximately equal to the 282 GPa theoretical elastic modulus.

The hardness values for samples fabricated at 40°C and -20°C were 16.78±0.43 GPa (1712.04±44.06 kg/mm^2) and 14.36±0.85 GPa (1465.46±86.26 kg/mm^2), respectively.

3.4. MICROSTRUCTURE

The SEM image of bars fabricated at -20°C revealed that several cracks spanned the entire bar (see Fig. 3.15). These cracks occurred because ice crystals formed at the boundary of each filament during freezing. Therefore, the boundaries of neighboring filaments were not strongly bonded, and only weak boundaries were connected, as shown in Fig. 3.15a. Fig. 3.16 shows an image of the side of a bar fabricated at -20°C, and this image indicates that ice crystal voids did indeed form.

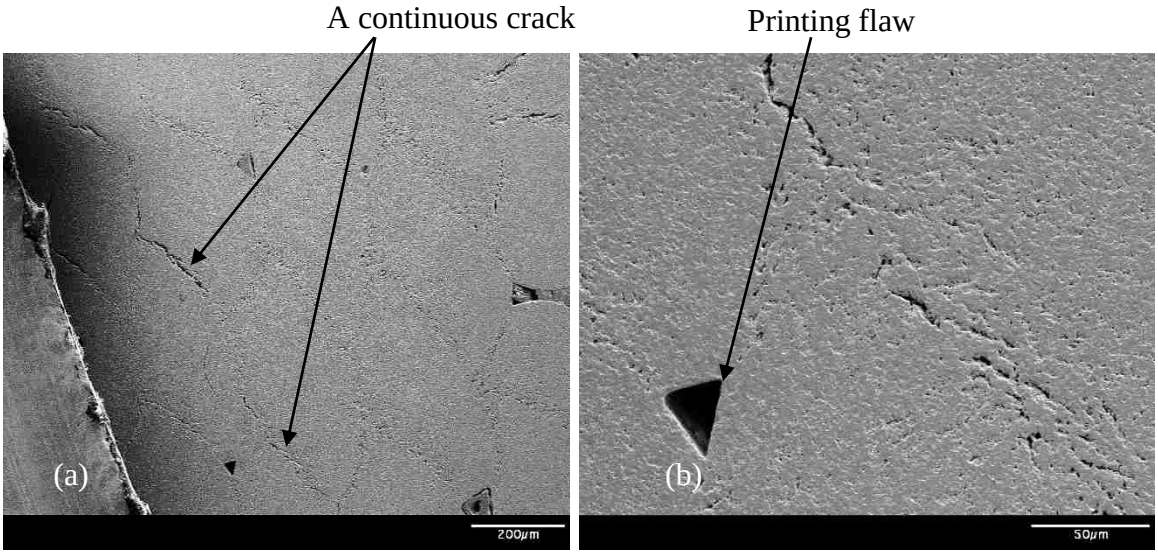

Figure 3.15. Cross-section of bars fabricated at -20ºC: (a) 100x zoom; (b) 350x zoom; (c) 350x zoom; and (d) 1,000x zoom

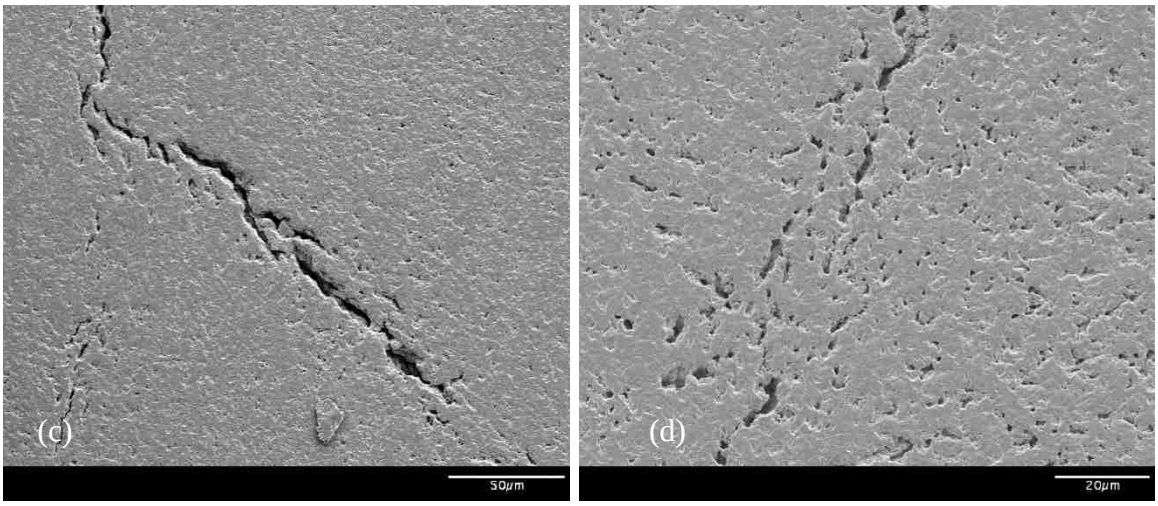

Figure 3.15 Cross-section of bars fabricated at -20ºC: (a) 100x zoom; (b) 350x zoom; (c) 350x zoom; and (d) 1,000x zoom (cont.)

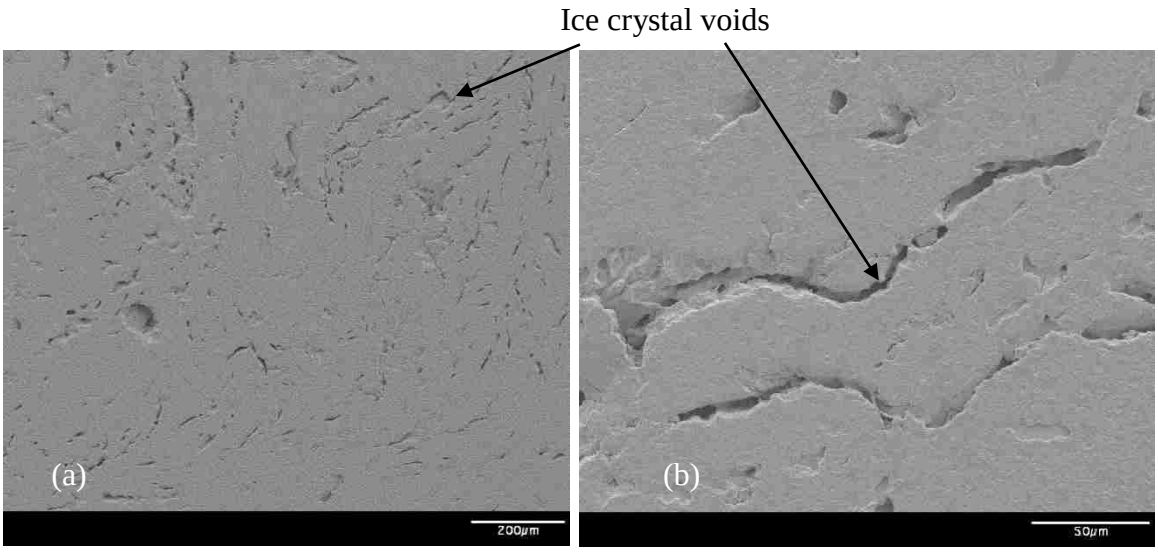

Figure 3.16. Side view of bars fabricated at -20ºC: (a) 100x zoom and (b) 350x zoom

Bars fabricated at -20°C without using a nozzle experienced a temperature gradient inside the filament before they were fully frozen. As noted in Section 3.1, a warmer temperature leads to additional formation of ice crystal voids. Figs. 3.18 and 3.17a, b show that the voids had larger sizes and that more voids were present than in bars fabricated at -20°C. The ice voids that formed displayed different morphologies

within one bar. The different morphologies relate to graded temperature, as shown in Figs. 3.17c (individual pores) and 3.17d (continuous pores). The SEM image of bars fabricated at a -20°C chamber temperature with a 0°C substrate temperature displays fewer ice crystal voids, but the ice crystal void size is considerably larger (see Fig. 3.19).

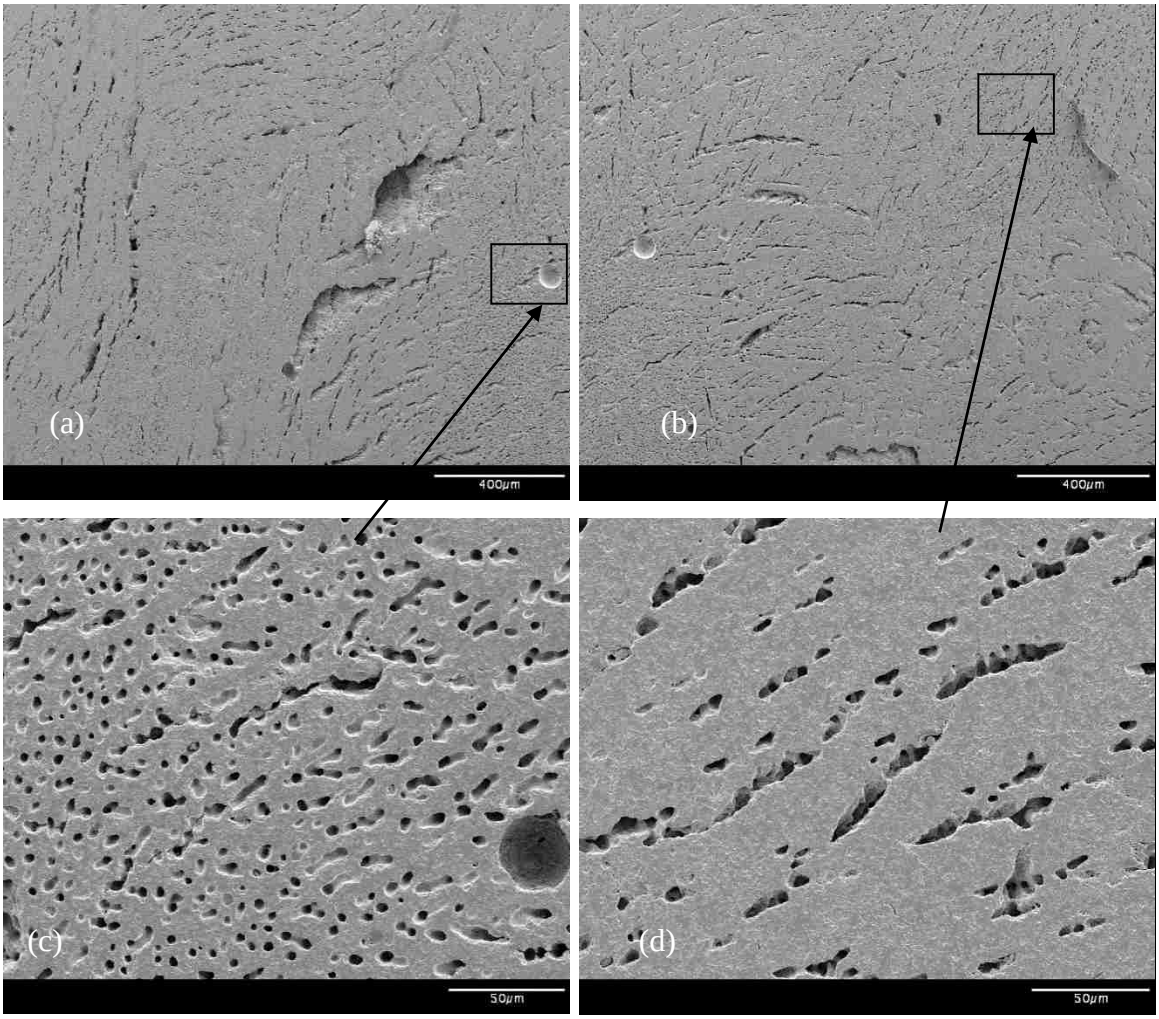

Figure 3.17. Side view of bars fabricated at -20°C without using a nozzle: (a) 70x zoom; (b) 70x zoom; (c) 350x zoom and (d) 350x zoom

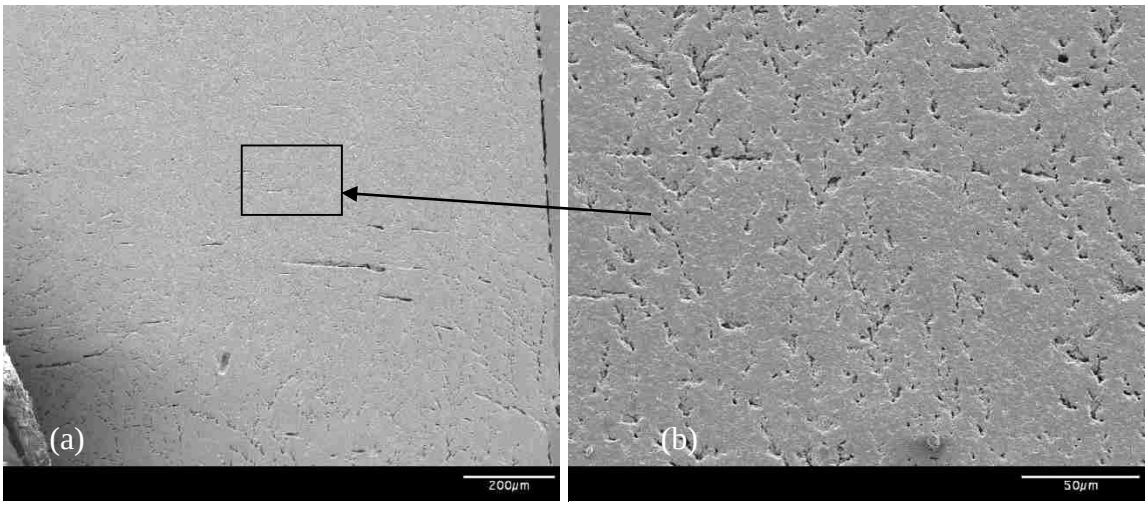

Figure 3.18. Cross-section of bars fabricated at -20ºC without using a nozzle: (a) 100x zoom and (b) 350x zoom

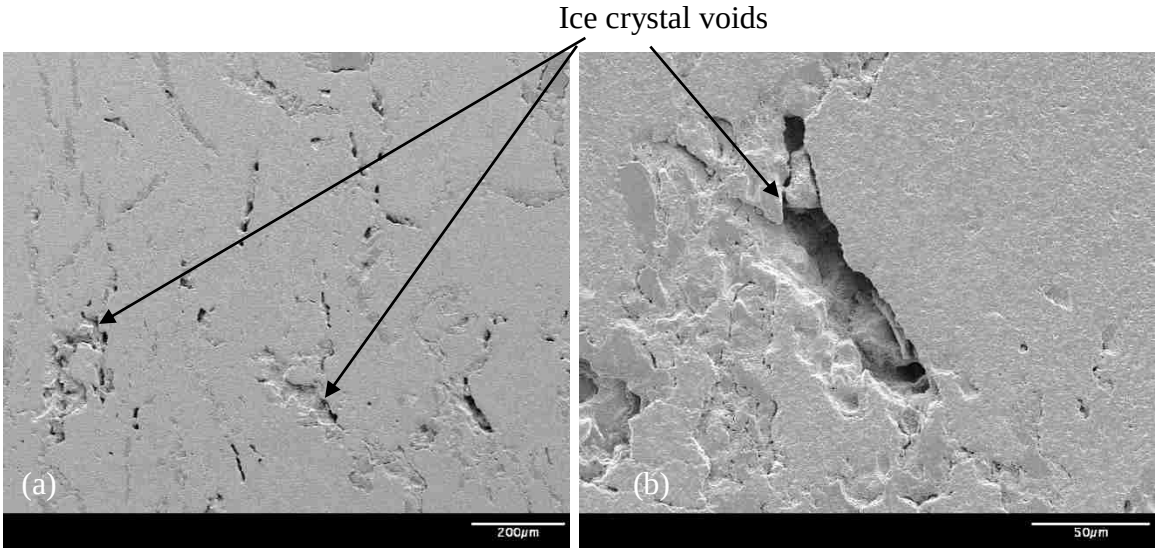

Figure 3.19. Side view of bars fabricated at a -20ºC chamber temperature with a 0ºC substrate temperature: (a) 100x zoom and (b) 350x zoom

The SEM images of bars fabricated at 40°C revealed the presence of air bubbles inside the bar (see Fig. 3.20a), and the microstructure was similar to that of pressed pellets, as illustrated in Figs. 3.20b and 3.21.

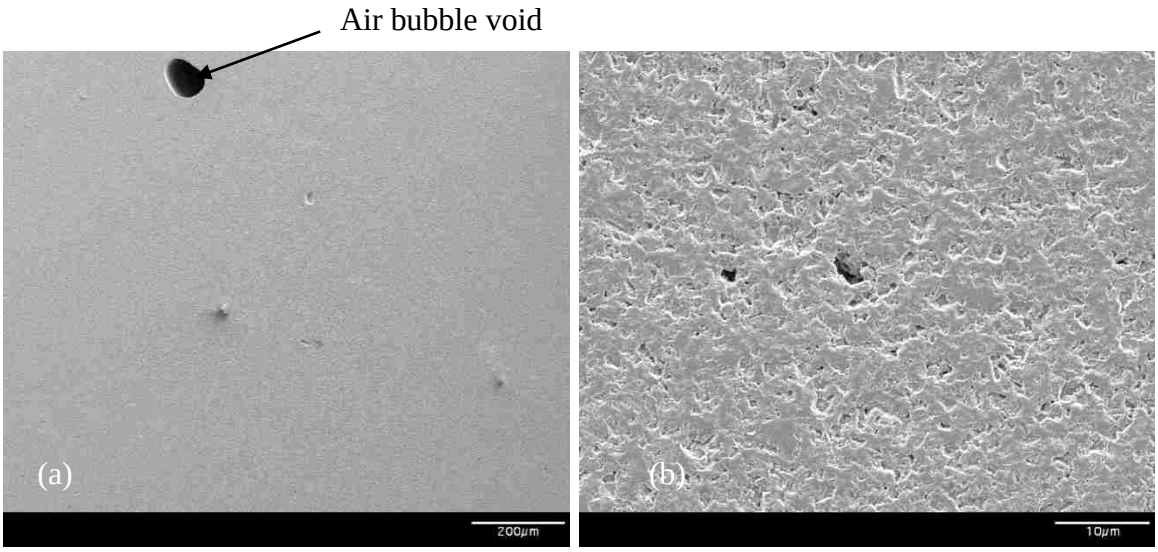

Figure 3.20. Cross-section of bars fabricated at 40°C: (a) 100x zoom and (b) 3,000x zoom

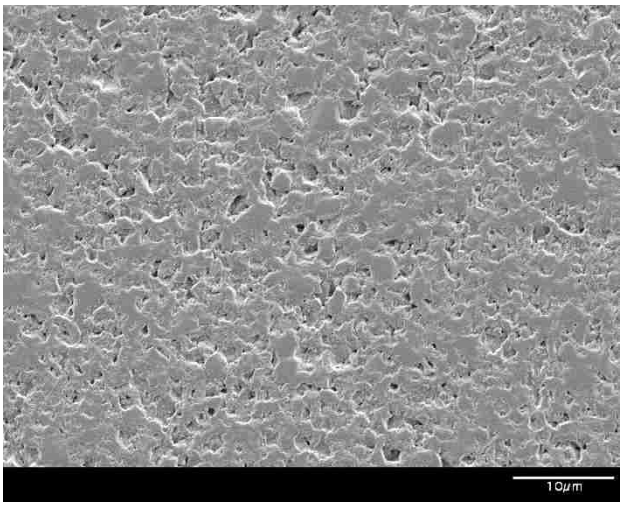

Figure 3.21. Cross-section of pressed pellet (3,000x zoom)

Based on the SEM images and optical images in Sections 3.1 and 3.3, the pore (ice crystal void) sizes were measured using Image J. Figs. 3.22a-c illustrate the amount of pores and pore size distribution for three different printing situations, and Fig. 3.22d shows the distribution difference in pore size among the three situations. These three printing situations were assumed as the three different temperature situations inside those

bars. Inside the bars fabricated at a -20°C chamber temperature with a 0°C substrate temperature, the temperature was closer to 0°C; the temperature inside bars fabricated at -20°C was closer to -20°C, and the temperature inside bars fabricated at -20°C without using a nozzle fell in between these two temperatures (approximately 14-15°C, see Fig. 3.7).

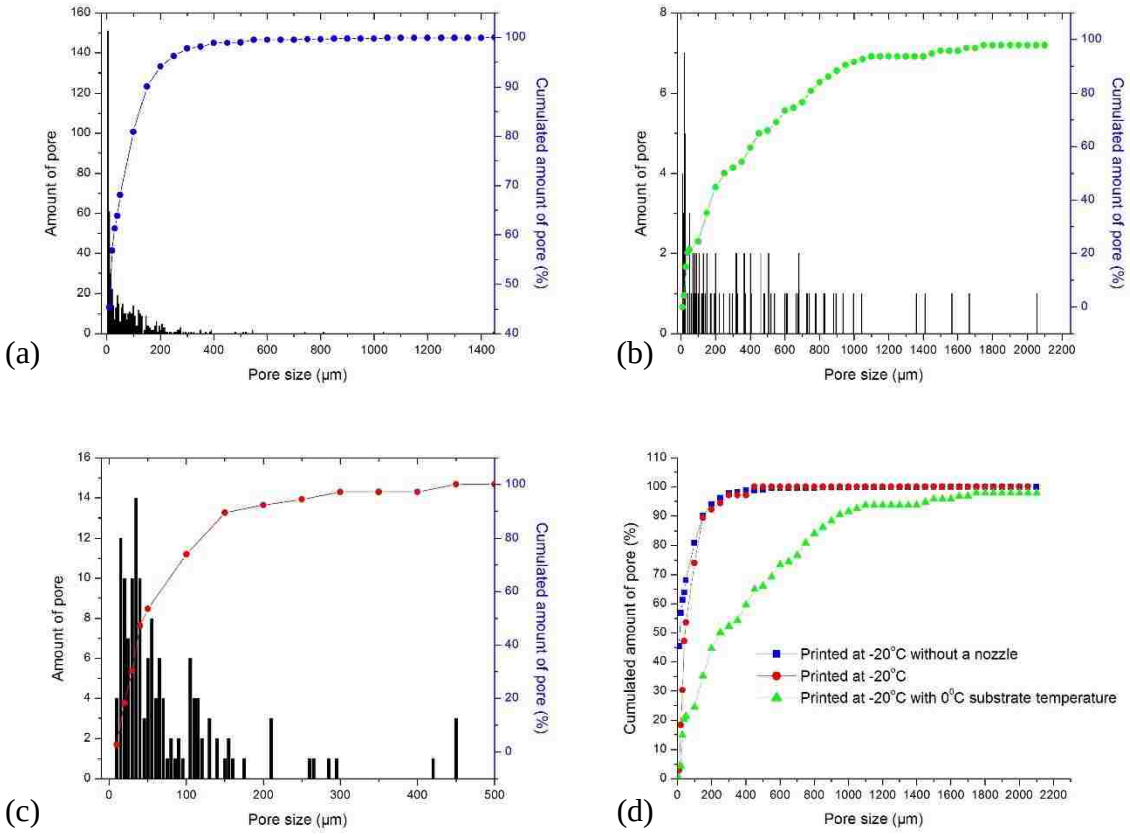

Figure 3.22 Pore size distribution of (a) bars fabricated at -20°C without using a nozzle; (b) bars fabricated at -20°C chamber temperature with a 0°C substrate temperature; (c) bars fabricated at -20°C and (d) comparison of the pore size distribution of the three different methods.

The bars fabricated at -20°C without using a nozzle exhibited a considerable amount of porosity in the range of approximately 50-100 μm, and 90% of the pores were smaller than 200 μm. However, a few pores (1%) were larger than 1,200 μm, which is a critical factor that affects the flexural strength. The bars fabricated at a -20°C chamber

temperature with a 0°C substrate temperature had fewer pores, but the pore sizes were considerably larger, with a pore size distribution from 5 to 2,000 μm. The bars fabricated at -20°C had a relatively uniform pore size, with 90% of the pores smaller than 150 μm. Based on Fig. 3.22d, the pore size shows the following tendency: in the range of 0°C to -20°C, the pore size increases with increasing temperature.

The growth of ice ejects the alumina particles to form an ice crystal with a different size and shape. After freeze-drying, the shape of the ice crystal remains in the part and forms ice crystal voids. The ice growth rate was different at different temperatures, and the different ice growth rates affect the ice pore size, i.e., faster freezing produces a smaller pore size [21, 22]. Based on the study of the microstructures and mechanical properties of bars fabricated at different temperatures, the ice crystal voids increased in size when the temperature is increased from -20°C to 0°C. These microstructure analysis results corroborate the statements in Section 3.1, i.e., the ice crystal voids that form at temperatures warmer than -20°C have a more negative effect on the mechanical properties than those formed at -20°C.

4. CONCLUSIONS

The work investigates the product properties and surface accuracy of Extrusion Freeform Fabrication at different fabrication temperature situations. Two satisfactory fabrication temperature situations were found, i.e., fabrication at a 40°C plate temperature inside a room temperature chamber and fabrication at a -20°C plate temperature in a -20°C temperature chamber.

The parts fabricated at 40°C achieved relative density, Young's modulus, flexure strength and hardness values of 96.73%, 311 GPa, 338 MPa and 16.78 GPa, respectively. At 40°C, the minimum deposition angle achieved was 50° at a 38 mm bottom diameter, and the parts experienced 7-14% shrinkage after sintering. The parts fabricated at -20°C attained relative density, Young's modulus and flexure strength values of 91.55%, 280 GPa and 300 MPa, respectively, and the hardness was 14.36 GPa. At -20°C, parts could be fabricated with a 24° minimum deposition angle at a 64 mm bottom diameter and displayed 10-16% shrinkage after sintering.

The slower drying of each filament at 40°C leads to a higher green body density for the part, resulting in a higher relative density and better mechanical properties, but the faster solidification of each filament at -20°C provides the ability to build a larger part without the use of support material. Analysis of the SEM images of parts obtained from Extrusion Freeform Fabricated aids in understanding the principle of ice crystal void formation at freezing temperatures.

APPENDIX

Recipe of 60% solids loading Al_2O_3 paste

1. Fill a 500 ml Nalgene bottle one-third of the way with Al_2O_3 media.
2. Weigh out 585 g of Al_2O_3 for the paste and pour them into the Nalgene bottle:
3. Use a graduated cylinder to measure 100 ml of deionized water.
4. Use a beaker and a scale to weigh out 5.50 g of Darvan C and 20 g glycerol.
5. Pour the Darvan C and glycerol into the Nalgene bottle. Use the 100 ml of water to rinse out the beaker into the Nalgene bottle.
6. Close the bottle and shake it by hand for a couple minutes until the contents make a slurry.
7. Ball mill for ~15 hours at ~35 rpm.
8. After ball milling, connect the water jacketed beaker to a water bath. Place the beaker on top of a stir plate. Set the water bath to 70°C. Do not remove the bottle off the ball mill until the water bath reaches 70°C.
9. Once the set temperature is reached, put a stir bar in the beaker and set it to speed 400 RPM. Pour the slurry into the water jacketed beaker. Make sure the media do not fall into the beaker.
10. Cover the beaker with a watch glass.
11. While waiting for the water bath temperature to come back to 70°C, weigh out 3.5 g of Methocel.
12. Lifting the watch glass with one hand, put a small amount of Methocel with a spatula in the other hand. Cover the beaker with the watch glass while the Methocel added is stirred into the slurry. Although the Methocel should be added slowly, the beaker should not remain uncovered for long since that will lead to water evaporation and the paste will not turn out as expected.
13. Once all the Methocel is added in, let the slurry stir for 5 minutes.
14. After 5 minutes, set the water bath to 20°C. Make sure to check on it every once in a while. If a layer starts forming, stir the slurry with the spatula. The paste will start setting. When the stir bar cannot possibly stir the paste, turn off the stir plate.

15. When the water bath reaches 20°C, use the spatula to put the paste in the Whip Mixer container. Close it with the lid. Connect the vacuum line. Turn it on. Whip mix it for 5 minutes. Using a cooking spatula, scrape the paste off the blade. Whip mix it for another 5 minutes. Let it cool for 2 minutes. Whip mix it another 5 minutes for a total of 15 minutes.
16. Disconnect the vacuum line. Turn the Whip Mix on for a minute to clean the line and lubricate the motor.
17. Using a cooking spatula, put the paste in a bottle. **Make sure to take a small sample for solid loadings calculation**

Recipe of 55% solids loading B_4C paste

1. Fill a 500 ml Nalgene bottle one-third of the way with ZrO_2 media about 760g;
2. Weigh out 300 g the B_4C powder for the paste and pour them into the Nalgene bottle;
3. Use a graduated cylinder to measure 100 ml deionized water and pour some more 20 ml water in the slurry as the compensation of water evaporation during the process;
4. Use a beaker and a scale to weigh out 2.4g of TMAH for the appropriate paste;
5. Close the bottle and shake it by hand until the contents turn into a slurry;
6. Ball mill for ~20 hours at ~35 rpm;
7. After ball milling, connect the water jacketed beaker to a water bath. Place the beaker at the bottom of a mechanical mixing machine. Set the water bath to 70°C. Do not remove the bottle off the ball mill until the water bath reaches 70°C;
8. Once the set temperature is reached, pour the slurry into the water jacketed beaker. Make sure the media does not fall into the beaker. Then, turn on the mixing machine and set it to a speed about 500;
9. Cover the beaker with a piece of plastic;
10. While waiting for the water bath temperature to come back to 70°C, weigh out 2.3g Methocel;
11. Lifting the plastic cover with one hand, put a small amount of Methocel with a spatula in the other hand. Cover the beaker with the watch glass while the Methocel added is stirred into the slurry, the speed of mixer could be adjusted

based on the mixing situation. Although the Methocel should be added slowly, the beaker should not remain uncovered for long since that will lead to water evaporation and the paste will not turn out as expected.

12. Once all the Methocel is added in, uncover the beaker about 7 mints for evaporate extra water, then cover the beaker and keep the mixing speed at speed about 500 and let the slurry stir for 5 minutes;
13. Set the water bath to 30°C. When the temperature lower than 45 °C, check on it every once in a while. If a layer starts forming, stir the slurry with the spatula quickly. The paste will start setting at ~40°C, then turn off the mechanical mixer and take off the stirring rod;
14. When the water bath reaches 30°C, use the spatula to put the paste in the Whip Mixer container. Close it with the lid and connect the vacuum line;
15. Turn the mixer on and mix it for 5 minutes, then using a cooking spatula, scrape the paste off the blade and let it cool for 2 minutes. After 2 minutes, mix it for another 8 minutes for a total of 15 minutes.
16. Disconnect the vacuum line. Turn the Whip Mix on for a minute to clean the line and lubricate the motor.
17. Using a cooking spatula, put the paste in a bottle. Close it with a lid preferably. **Make sure to take a small sample for solid loadings calculation**

BIBLIOGRAPHY

1. Jacobs, P. F., *Rapid prototyping and manufacturing: fundamentals of stereolithography*, 1st Ed., Society of Manufacturing Engineers (1992).

2. Guo, N., and Leu, M. C., "Additive manufacturing: technology, applications and research needs," *Frontiers of Mechanical Engineering*, Vol. 8, No. 3, Pp. 215-243 (2013).

3. Noguera, R., Lejeune, M., and Chartier, T., "3D fine scale ceramic components formed by ink-jet prototyping process," *Journal of the European Ceramic Society*, Vol. 25, No.12, Pp. 2055-2059 (2005).

4. Griffith, M. L., and Halloran, J. W., "Freeform fabrication of ceramics via stereolithography," *Journal of the American Ceramic Society*, Vol. 79, No. 10, Pp. 2601-2608 (1996).

5. Grau, J., Moon, J., Uhland, S., Cima, M. J., and Sachs, E., "High green density ceramic components fabricated by the slurry-based 3DP process," In *Solid Freeform Fabrication Symposium*, Pp. 371-378 (1997).

6. Lewis, J. A., Smay, J. E., Stuecker, J., and Cesarano, J., "Direct Ink Writing of Three-Dimensional Ceramic Structures," *Journal of the American Ceramic Society*, Vol. 89, No. 12, Pp. 3599-3609 (2006).

7. Griffin, E. A., and McMillin, S., "Selective laser sintering and fused deposition modeling processes for functional ceramic parts," In *Proceedings of the Solid Freeform Fabrication Symposium*, Vol. 6, Pp. 25-30 (1995).

8. Cesarano, J., "A review of robocasting technology," In *MRS Proceedings*, Cambridge University Press, Vol. 542, Pp. 133. (1998).

9. Agarwala, M. K., Jamalabad, V. R., Langrana, N. A., Safari, A., Whalen, P. J., and Danforth, S. C., "Structural quality of parts processed by fused deposition," *Rapid Prototyping Journal*, Vol. 2, No. 4, Pp. 4-19 (1996).

10. Lous, G. M., Cornejo, I. A., McNulty, T. F., Safari, A., and Danforth, S. C., "Fabrication of piezoelectric ceramic/polymer composite transducers using fused deposition of ceramics," *Journal of the American Ceramic Society*, Vol. 83, No. 1, Pp. 124-28 (2000).

11. Denham, H. B., Cesarano III, J., King, B. H., and Calvert, P., August, "Mechanical behavior of robocast alumina," In *Proceedings of the Solid Freeform Fabrication Symposium*, Pp. 589-596 (1998).

12. Huang, T., Mason, M. S., Zhao, X., Hilmas, G. E., and Leu, M. C., "Aqueous-based freeze-form extrusion fabrication of alumina components," *Rapid Prototyping Journal*, Vol. 15, No. 2, Pp. 88-95 (2009).

13. Huang, T., Mason, M. S., Hilmas, G. E., and Leu, M. C., "Freeze-form extrusion fabrication of ceramic parts," *Virtual and Physical Prototyping*, Vol. 1, No. 2, Pp. 93-100 (2006).

14. Rahaman, N., *Ceramic processing*. 1st Ed., John Wiley & Sons, Inc., (2006).

15. Singh, B. P., Bhattacharjee, S., Besra, L., and Sengupta, D. K., "Evaluation of dispersibility of aqueous alumina suspension in presence of Darvan C," *Ceramics international*, Vol. 30, No. 6, Pp. 939-946 (2004).

16. Saravanan, L., and Subramanian, S., "Surface chemical studies on the competitive adsorption of poly (ethylene glycol) and ammonium poly (methacrylate) onto alumina," *Journal of colloid and interface science*, Vol. 284, No. 2, Pp. 363-377 (2005).

17. Sofie, S. W., and Dogan, F., "Freeze casting of aqueous alumina slurries with glycerol," *Journal of the American Ceramic Society*, Vol. 84, No. 7, Pp. 1459-1464 (2001).

18. Zhao, X. Y., Mason, M. S., Huang, T. S., Leu, M. C., Landers, R. G., Hilmas, G. E., Easley, S. J, and Hayes, M. W., "Experimental Investigation of Effect of Environment Temperature on Freeze-Form Extrusion Fabrication," In *18th Annual Solid Freeform Fabrication Symposium*, Pp. 6-8 (2007).

19. Wachtman, J. B., Cannon, W. R., and Matthewson, M. J., *Mechanical properties of ceramics*, 2nd Ed., John Wiley and Sons (2009).

20. Richerson, D., *Modern ceramic engineering: properties, processing, and use in design*, 3rd Ed., CRC press (2005).

21. Deville, S., "Freeze-Casting of Porous Ceramics: A Review of Current Achievements and Issues," *Advanced Engineering Materials*, Vol. 10, No. 3, Pp. 155-169 (2008).

22. Deville, S., Saiz, E., and Tomsia, A. P., "Ice-templated porous alumina structures" *Acta Materialia*, Vol. 55, No. 6, Pp. 1965-1974 (2007).

VITA

Jie Li was born on April, 1990 in Beijing, P. R. China. In July 2012, he received his Bachelor of Science degree in Material Forming and Control Engineering from North China University of Technology, Beijing, P. R. China. In August 2012, he began his study for Master's degree in Mechanical and Aerospace Engineering. His research areas include manufacturing, solid freeform fabrication, and ceramic processing. In May 2015, he received his Master's degree in Mechanical and Aerospace Engineering from Missouri University of Science and Technology. After his graduation, he will continually dedicate himself in the field of mechanical engineering.